Mechanochemical Synthesis of Tungstophosphoric Acid Based High Efficiency Photocatalysts

Syed Waqar Hussain Shah[a*], Omama Zafar[a], Irum Bibi[a], Saifullah Zafar Khan[b], Sadaf Bibi[c], Kashif Ali[d]

[a]*Department of Chemistry, Hazara University, Mansehra, Pakistan*

[b]*Abbottabad University of Science and Technology Havelian, Pakistan*

[c]*Beijing Institute of Technology, China*

[d]*Hubei University Wuhan, China*

syedwhshah@gmail.com

Keywords: *tungstophosphoric acid, photocatalysis, dye degradation, mechanochemical, proton-transfer.*

Organic-inorganic hybrids (WT) based on tungstophosphoric acid (TPA) and tris(hydroxymethyl)aminomethane (TRIS) were synthesized by a sustainable, solventless, mechanochemical route. SEM and Powder X-ray diffraction (PXRD) showed a shift from bulk crystallinity in TPA to nanocrystalline domains in WT. Rietveld refinement revealed an expansion of Keggin unit upon hybrid formation. Proton transfer and alteration in H-bonding interactions were established through ATR-IR spectroscopy. WT had higher thermal stability compared to TPA. Under solar irradiation, a superior malachite green (MG) removal ranging from 92.5 – 98.5% was achieved with 1.2 g of WT. This work discusses the modification of polyoxometalates for high-performance light-aided catalysis.

Introduction

Keggin type, heteropoly Brønsted acid, and polyoxometalate tungstophosphoric acid (TPA) show reversible redox properties [1]. They are water soluble, exhibit low surface area (<10 m^2/g), and are not significantly thermally stable, which limits their use [2]. However, it is possible to design stable organic-inorganic hybrids by replacing the proton of TPA with an organic cation. These alterations in the structural features lead to better stability and catalytic performance [3–6].

Tris(hydroxymethyl)aminomethane or TRIS is a biocompatible base, possessing both amino and hydroxyl groups that can form dense H-bonded network with terminal and bridging atoms in the Keggin unit [7]. The greater charge separation caused by modified electron environment is expected to favour photocatalysis [3,8–10].

Mechanochemical or solvent-less synthesis is a green alternative to the traditional methods used for the fabrication of hybrid ionic solids. In addition to eliminating the need for toxic organic media, grindstone activation breaks down bulk crystals into nano-sized domains, thus facilitating solid-state proton transfer [10–12].

In this work, we demonstrate the mechanochemical fabrication of organic-inorganic hybrids based on TRIS and TPA by systematically varying the mole fractions of acid and base from 0.1 to 0.9. They were characterized using attenuated total reflectance Fourier transform infrared spectroscopy, powder X-ray diffraction, scanning electron microscopy, and thermogravimetric analysis. Their catalytic performance for the removal/degradation of malachite green dye under renewable solar irradiation was also evaluated. The eco-friendly and facile synthesis of photocatalysts with remarkable efficiency for pollutant degradation using renewable energy from the sun makes the process of environmental remediation cost-effective.

Experimental part

Material

Tris(hydroxymethyl)aminomethane (TRIS, 99.9%), tungstophosphoric acid (99.995%), and malachite green (dye content > 90%) were purchased from Sigma-Aldrich. Ultrapure water from a High-Milli-Q Advantage A10 System (Millipore, France) was used for the dye degradation study.

Synthesis of hybrids (WT)

Five binary mixtures (WT1–WR9) were prepared between tris(hydroxymethyl) aminomethane and tungstophosphoric acid through systematic variation in the mole fraction. Each mixture was subjected to mechanochemical activation and thermal treatment in thoroughly dried capped vials. After allowing 3-4 h for completion, the product was allowed to reach ambient temperature and stored in a moisture-free atmosphere. The mole fraction of TRIS was 0.1, 0.2, 0.5, 0.8, and 0.9 in WT1, WT2, WT5, WT8 and WT9, respectively. The last digit in the names reflects the mole fraction of TRIS in the hybrid. WT1 and WT2 had some aqueous solubility, whereas the remaining hybrids did not dissolve in water.

Characterization of Hybrids

TPA-TRIS hybrids (WT) were characterized using powder X-ray diffraction (Siemens D-5000 diffractometer) with Cu Kα radiation (λ = 1.5406 Å). Scanning electron microscopy (SEM) images were captured using a Hitachi S-4800 instrument. ATR-IR spectra were recorded on a Perkin Elmer Spectrum 3 spectrometer. Thermogravimetry was performed with a Perkin Elmer STA 8000 under a N_2 atmosphere. The temperature varied at a rate of 10°C/min during measurement. Origin 9.0 and Xpert highscore plus v. 3.0, were used for data processing. The SEM images were analyzed using ImageJ software (NIH).

Light aided dye degradation

For the photocatalytic degradation of MG, a stock solution of 1.0 mM was prepared and diluted to obtain lower concentrations of 0.5 and 0.1 mM. Each solution was sonicated for 15 min for homogenization. The sunlight exposure time was 1 h. No cutoff filters were used for the wavelength selection. Each solution was filtered to remove any solid particles before absorbance was recorded at λ_{max} (MG) = 617 nm [13]. The experiments performed in the absence of light showed insignificant changes in the absorbance.

The foundational performance of hybrids was evaluated using absolute degradation percentage of MG using three different dye concentrations (0.1 mM, 0.5 mM and 1.0 mM). The quantity of catalyst varied from 0.4 g to 2.0 g. The hybrids were compared with TPA using different performance indicators. Apparent rate constants (k_{app}) for pseudo-first order kinetics, synergy index (SI), specific degradation rate (SDR), and adsorption constants (K_{ads}) using Langmuir-Hinselwood (L-H) model were computed for each system [14–17].

Results and discussion

Attenuated total reflectance infrared spectroscopy

ATR-IR spectra of TRIS and its hybrids (WT1-WT9) are shown in **Figure 1** and their partial magnified spectra covering different frequency regions are provided in supplementary **Figure S1**. The corresponding vibrational frequencies are provided in supplementary **Table S1**. The region (**Figure S1-A**) represents a transition from self-associated organic crystal to complex ion-pair supramolecular assembly. TRIS shows a triplet in this region at 3174, 3287, and 3339 cm^{-1}. The peaks are the symmetric and asymmetric stretching modes of the $-NH_2$ and -OH groups locked into a crystalline order. Upon introduction of TPA, the TRIS-TRIS hydrogen bonding network is disrupted and replaced by a TRIS-anion hydrogen bonding. This leads to high frequency peaks in the region 3480 – 3530 cm^{-1}.

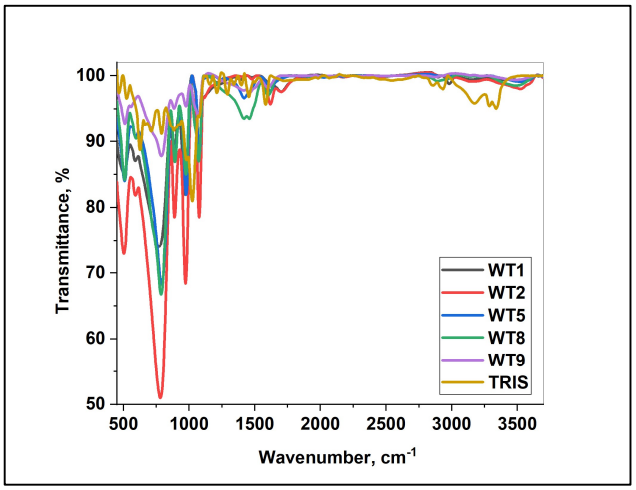

Figure 1. ATR-IR spectra of TRIS and its hybrids (WT) with TPA.

Since the Keggin anion (~12Å) acts as an enormous spacer, the TRIS molecules can no longer reach each other to form tight, ordered bonds [18]. They are weakly interacting with the oxygen atoms of TPA surface. The broad and shallow humps seen in the region 3000-3300 cm^{-1} is the signature of protonation. While $-NH_2$ gives sharp peaks, $-NH_3^+$ exhibits a broad band reflective of different environments in which these new N-H bonds exist as they interact with different oxygen sites of the acid. The bands may be completely absent if there are symmetry constraints [19,20]. The conclusive evidence of proton transfer is provided by the alteration of spectral patterns in the region 1540-1800 cm^{-1} (**Figure S1-B**). In TRIS, $\delta(NH_2)$ = 1583 cm^{-1}, and in hybrids (WT1, WT2, and-WT5) $\delta_{as}(NH_3^+)$ is localized at 1619 cm^{-1}. In WT8 and WT9 having excess of TRIS, a peak at ~ 1601 cm^{-1} reflects mixed $\delta(NH_2/NH_3^+)$ mode [10,21]. Here, a classical Bronsted acid-base reaction is occurring.

$$[H_3PW_{12}O_{40}] + n[TRIS] \rightarrow [n(TRIS\text{-}H)^+ \cdot (H_{3-n}PW_{12}O_{40})^{n-}]$$

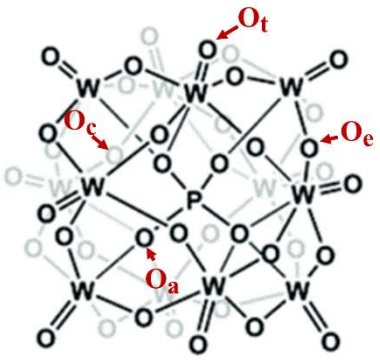

Figure 2. Keggin structure of tungstophosphoric acid, showing different types of oxygen atoms: terminal oxygen (O_t); central oxygen (O_a); corner sharing (O_c); and edge sharing (O_e). Adapted from [20].

The hydration signal observed at 1701 cm^{-1} in WT1 and WT2 is due to hydronium ions (H_3O^+) or Zundel ions ($H_5O_2^+$) as protons exist in this form in pure TPA [22–24]. They are not found in WT5, WT8, and WT9 due to shifting of proton to TRIS.

The shift in C-H stretching observed in the region 2750-3050 cm^{-1} shows the stiffening of bonds due to inductive de-shielding caused by NH_2 protonation (**Figure S1-C**). The broadening suggests a high degree of environmental heterogeneity. The C-N bond that vibrates at 1211 cm^{-1} in TRIS appears at 1240 cm^{-1} in hybrids WT1 and WT2 (**Figure S1-D**). In acid-rich hybrids, TRIS exists predominantly in the cationic state, and the inductive pull of NH_3^+ stiffens the C-N bond [10]. The strong electrostatic clamping of protonated TRIS with $[PW_{12}O_{40}]^{3-}$ results in cation stabilization. The effect is diluted when TRIS is in excess and TRIS molecules can form hydrogen bonds with themselves too. The CH_2 scissoring, rocking and twisting peaks appear in the range 1200-1535 cm^{-1} alongside δ(OH). The hybrids exhibit significantly broadened and shifted peaks in this range, which indicates that CH_2 groups are no longer in the identical environment.

Finally, the analysis of peaks in the range 700-1100 cm^{-1} (**Figure S1-E & F**) shows the retention of the primary Keggin structure as shown in **Figure 2** [25,26]. $\nu_{as}(P\text{-}O_a)$ band representing the central tetrahedron is negligibly shifted and the peak ~ 1075 cm^{-1} is stable across all hybrids saving WT9 that appears at 1070 cm^{-1} [22]. With excess TRIS, the symmetry breaking and distortion of phosphate core is expected. $\nu_{as}(W{=}O_t)$ band originally at 980 cm^{-1} is also red-shifted by a magnitude of 3-10 cm^{-1}. The peak shift and broadening indicate electrostatic interaction between $TRISH^+$ and these terminal oxygen atoms [27]. $\nu_{as}(W\text{-}O_c\text{-}W)$ is localized at 886 cm^{-1} in TPA [22]. A shift in this band from 886 to 891 cm^{-1} represents cation-anion synergy. O_c acts like a bridge connecting four W_3O_{13} triplets. The residence of TRIS cation between these triplets makes these bridges hard to vibrate and frequency goes up. Also, the electrostatic interactions prevents an effective H-bonding and W-O-W are not elongated as in the case of TPA [20]. At this stage, the phosphate distortion occurs (as established earlier in this discussion) and strain is released, resulting in shift of frequency back to 885 cm^{-1} in WT9. For edge sharing oxygen, $\nu_{as}(W\text{-}O_e\text{-}W)$ exists as 771 cm^{-1} for WT1. It shifts to higher frequencies with increase in TRIS content in the hybrid. The region is complex because NH_2 wagging and

skeletal vibrations appear at 790 cm^{-1}. The red

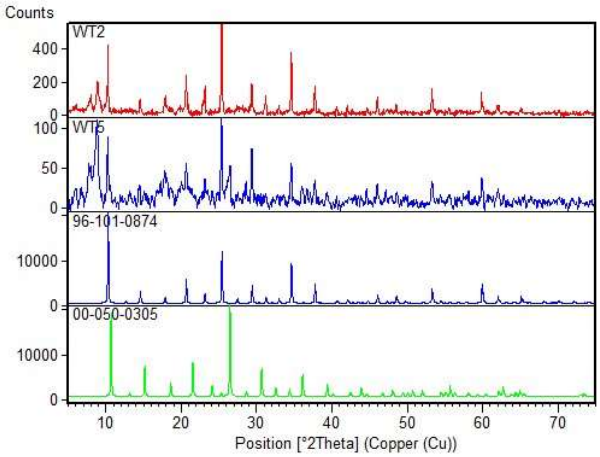

Figure 3**.** X-Ray diffractograms for selected TPA-TRIS hybrids (WT2 and WT5) and their comparison with standard and tungstophosphoric acid (JCPDS 101-0874) and ammonium phosphotungstate (JCPDS 50-0305).

shift of 19 cm^{-1} is due to TRIS protonation. Based on the shifts in this region, one can safely conclude that the hybrids are not engaged in hydrogen bonding similar to that existing in the hydrated TPA [20]. The Keggin skeletal vibrations (500 cm^{-1}) are negligibly shifted in WT1-WT5, showing the stability of inorganic cage. The $\Delta\nu = 6$ cm^{-1} for WT8 where the electrostatic pressure causes structural compression and breathing occurs at higher frequency. The signal is diluted in the presence of excess TRIS. The Internal $W{-}O_a{-}P$ mode (500 cm^{-1}) is blue shifted from 502 to 511 cm^{-1} from WT1 to WT9. When the skeleton is squeezed, the bonds between the phosphate core and tungsten triplet get shorter and stiffer, therefore the corresponding vibrational frequencies go up.

Powder x-ray diffraction analysis

X-Ray diffraction patterns of WT2 and WT5 are shown in **Figure 3**. Matching was performed with the standard TPA (JCPDS 101-0874) and its ammonium salt APT (JCPDS 50-0305). The profile matching (supplementary **Tables S2 and S3**) showed that the Keggin features remain intact in the hybrids, where reflections below 2θ value of 10° may represent superlattices, or hydrated/intercalated phase [28–31]. Furthermore, the structural information on hybrids was extracted using Rietveld Refinement. The results are provided in supplementary **Table S4**. PXRD data confirmed that incorporation of TRIS molecules caused the expansion of $Pm\bar{3}n$ unit. Apparently, the partial substitution of H_3O^+ by organic $C_4H_{12}NO_3^+$ necessitates the physical widening of the inorganic framework [10,32–35]. In WT2 a volumetric expansion of 1.89% compared to TPA was observed. However, the lattice constant *a* decreased from 12.217 Å to 12.206 Å from WT2 to WT5. This signifies that while the TRIS molecules are forcing the lattice to stay expanded, the increased TRIS density is pulling the framework back together causing 0.27% volume reduction compared to less-saturated WT2 (supplementary **Table S5**). This corelates with blue shifts seen in the W-O-W and W-O-P modes in the IR spectra. The stiffening in WT5 is evident from shortening of W-O bond length (to 2.169 Å) and elevated microstrain (4.47×10^{-3}). The high density of interfacial hydrogen bonding leads to more integrated composite [36]. This is reflected by more stable Rietveld fit (R_{wp} = 18.06% and χ^2 = 1.98). However, the tightening

of the lattice is not perfectly uniform compression, rather it leads to twisting of WO_6 octahedra as distortion index increased from 0.2178 in WT2 to 0.2183 in WT5 [20,34]. The crystallite sizes ranging between 51-60 nm for WT2 and WT5 obtained using Scherrer and Williamson-Hall microstructural analyses [37] confirmed the nanostructuring of bulk TPA via mechanochemical activation. The high surface-to-volume ratio allows maximum interfacial hydrogen bonding at the organic-inorganic interface. The resulting molecular corset exerts inward mechanical pressure to cause limited lattice contraction. Obviously, while small distortion is favourable to accommodate hydrogen bonding, pushing the bonds beyond their ideal coordinates would make the process energetically non-feasible.

Thermogravimetry

Thermograms of the TPA-TRIS hybrids (WT) are shown in **Figure 4**. WT2 (TPA:TRIS = 4:1) showed minor degradation of 2.14% (i.e., due to water loss and TRIS degradation), which may be attributed to high thermal stability of predominant TPA [38,39]. The base-rich WT8 was decomposed to an extent of 17.84% overall. Below 200°C (stage I), dehydration occurred with mass loss of ~ 3%. The protonation of TRIS converts hydronium ions to free water. In the temperature range 200-580°C (stage II), the decomposition of organic components resulted in a mass reduction of further 9.74%. In WT8, TRIS exists in protonation as well as in free state and hence multiple thermal events are expected.

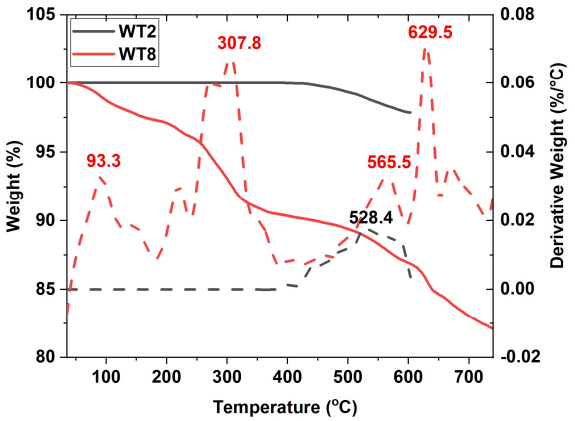

Figure 4. Thermogravimetric analysis of selected TPA-TRIS hybrids (WT2 and WT8). The corresponding derivative plots (DTG) are shown by dashed lines.

The peak at 629.5°C in DTG of WT8 indicates the collapse of the Keggin unit into stable oxides of tungsten and phosphorous during stage III [40,41]. Similar to parent TPA, the hybrids exhibited high thermal stability and a significant residual mass of ~ 98% and 82% was maintained in the case of WT2 and WT8, respectively [38].

Scanning electron microscopy

Further insight into the structural features of mechanochemically synthesized hybrids was provided by comparing the SEM image of TPA with that of WT5 (**Figure 5**). There is a morphological transformation from large dense TPA aggregates (4A) to tiny particles in WT5 (4a-d), which indicates that milling not only causes proton transfer in the solid state but also breaks down the macrostructures and prevents the re-growth of large crystals owing to the capping effect of TRIS. This validates the findings of XRD analysis. TPA has large non-uniform block-like crystals with sharp edges and particle sizes exceeding 10 μm.[42]

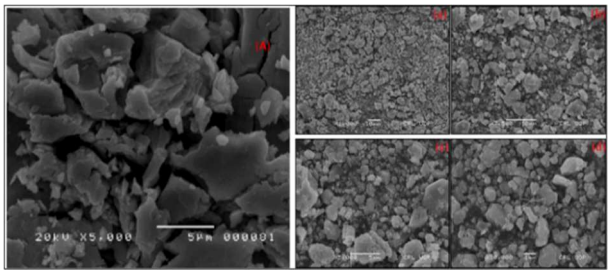

Figure 5. Scanning electron microscopy images of (A) tungstophosphoric acid (TPA); (a-d) PTA-TRIS hybrid WT5 at different magnification. The image of TPA is adopted from ref [42].

The surface texture is smooth with crystalline facets. In contrast, WT5 comprises uniform, spherical, or plate-like nanoaggregates, forming a rough and porous surface. The low-magnification images of WT5 show a uniform distribution of secondary aggregates. High magnification reveals that these aggregates are composed of small primary nanoparticles. This hierarchy, which is typical of organic-inorganic hybrids and correlates perfectly with the XRD results [34].

Photocatalytic dye degradation

Finally, the photocatalytic removal of malachite green (MG) by the hybrids (WT) was investigated. The mathematical relationships and data on percent dye removal and kinetic parameters is provided in supplementary **Tables S6-S8**.

Effect of catalyst dose

The quantity of catalyst has a direct effect on the dye removal. However, it is limited by the properties of suspension and aqueous solubility. For water-insoluble hybrids (WT5, WT8 and WT9), MG removal follows a parabolic curve. A removal of 97.47% was achieved with 0.5 mM dye and 1.6 g of WT8, which mirrors the maximum apparent rate constant (k_{app}) of 0.0612 min^{-1}. As more active sites are available with greater quantity of catalyst, so removal is facilitated. The removal declines to 93.61% when WT8 is increased to 2.0 g, which is due to enhanced turbidity of the medium that reduces photon-flux. In contrast to removal percentages, the total degradation rate proves that lower catalyst doses are more efficient. For instance, SDR peaks at 2.236 $mmol.g^{-1}.h^{-1}$ for 0.4 g of WT8, with 89.43% removal of 1.0 mM MG compared to SDR of 0.808 for 1.2 g catalyst with 97.05% dye removal (**Figure 6**). For pure TPA, the removal of 0.1 mM MG increases from 62.15% to 81.20% when catalyst quantity is changed from 0.4 g to 1.6 g.

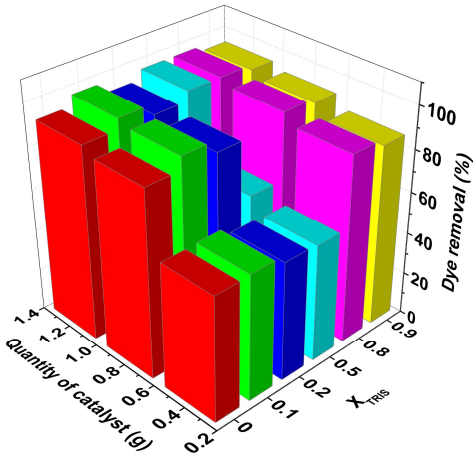

Figure 6. The effect of catalyst dose on removal of 1.0 mM MG dye by pure TPA and its hybrids possessing different mole fractions of TRIS.

With partially soluble WT1/WT2 the adsorption constant (K_{ads}) remains low due to absence of stable solid surface. The magnitudes of K_{ads} differ widely for 0.1 mM dye between WT1 (0.015) and WT9 (0.061). On the other hand, k_{app} remains high due to high collision frequency in the dissolved state. When MG concentration is changed from 0.1 mM to 0.5 mM, the removal improves from 61.79% to

96.97% with WT2 (**Figure 7**), since the increased chemical potential forces the dye to interact with catalyst more effectively. When x ≥ 0.5, the K_{ads} is significantly enhanced because the active sites concentrated at the solid interface are more efficient at trapping dye molecules [13].

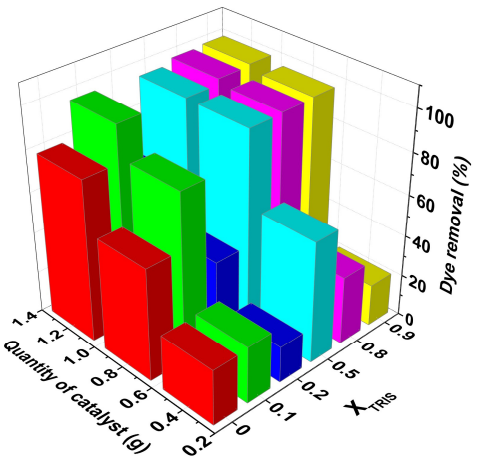

Figure 7. The effect of catalyst dose on removal of 0.1 mM MG dye by pure TPA and its hybrids possessing different mole fractions of TRIS

Effect of dye concentration

At low dye concentration k_{app} is generally at its peak (for example 0.0696 min^{-1} for WT9) because the ratio of dye to active sites is low, and dye molecules are attacked by ROS [43]. Though the physical removal remains high, the k_{app} either remains stable of declines due to delayed processing caused by the dye overload. For pure PTA, SDR rises from 0.065 to 0.772, when MG concentration increases from 0.1 mM to 1.0 mM.

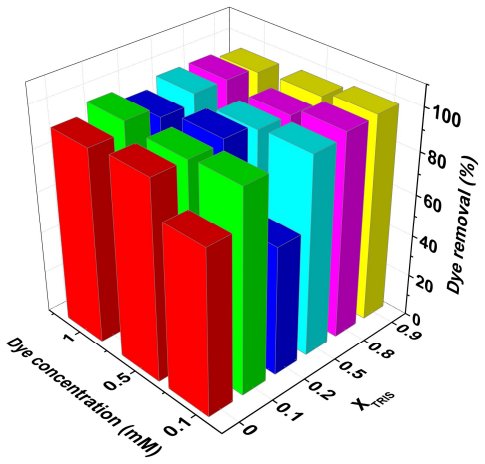

Figure 8. Effect of different dye concentrations on removal of MG dye by 1.2 g of TPA and its hybrids possessing different mole fraction of TRIS.

Similar trends are seen with hybrids. For completely soluble PTA, K_{ads} increased negligibly from 0.003 mM^{-1} to 0.009 mM^{-1} with increase in dye concentration. For insoluble WT9, it changed from 0.061 to 0.070 for 1.2 g catalyst, showing the surface saturated at high MG concentrations. For soluble hybrid WT2, the removal was elevated at high dye concentration (**Figure 8**), but strictly insoluble hybrids (WT5, WT8, WT9) maintained high removal percentages regardless of whether MG concentration was low or high [44].

Nature of catalyst

The percent removal data is conclusively evident that functional of TPA creates a superior catalytic architecture, driven by a critical phase transition from soluble to insoluble. The solubility translates directly to higher removal percentages. For 1.2 g catalyst and 0.1 mM MG, the removal is elevated from 78.71% for pure TPA to 98.46% for insoluble WT9 framework. The yields a synergy index (2.70) which is nearly three folds as that of TPA. While soluble hybrids struggle to establish a strong adsorption (K_{ads} =

0.004 to 0.015 for 0.1 mM MG), the insoluble WT9 achieves a K_{ads} of 0.061 securing a 98.46% removal [7]. Overall, the organic-inorganic hybrids surpassed similar materials in terms of efficiency in sunlight-aided catalysis [3,4,10,13,44].

Mechanism of catalysis

The mechanism of sunlight-aided degradation using ionic solids is expected to involve the following steps [13].

i) Photoexcitation

$$[PW_{12}O_{40}]^{3-} + h\nu \rightarrow [PW_{12}O_{40}]^{3-*}(h^+_{vb} + e^-_{cb})$$

(i) Charge stabilization

$$[TrisH]^+ + e^-_{cb} \rightarrow [TrisH \ldots e^-]$$

(ii) ROS generation

$e^- + O_2 \rightarrow \cdot O_2^-$ (superoxide)

$h^+ + H_2O \rightarrow \cdot OH + H^+$ (hydroxyl radical)

$\cdot O_2^- + H^+ \rightarrow \cdot HO_2 \rightarrow \cdots \rightarrow \cdot OH$(secondary radicals)

(iii) Malachite green mineralization

$$G^+ + \cdot OH / \cdot O_2^- \rightarrow \text{Intermediates} \rightarrow CO_2 + H_2O + NO_3^-$$

Conclusions

The comprehensive morphological and catalytic evaluation of TPA-TRIS hybrids confirm a transition from soluble phase to high-performance heterogenous system. ATR-IR spectroscopy varied the retention in the Keggin framework while surrounded by a stable organic-cationic environment. Rietveld refinement showed a 1.89% expansion in unit cell for WT2, enhancing the surface-active geometry upon TRIS incorporation. A superior catalytic efficiency with 98.46% dye removal was achieved with 0.1 mM MG and WT9. A parabolic relationship was found between efficiency and catalyst dose, where maximum efficiency was achieved with an optimal load of 1.6 g. Kinetically, the hybrids outclass pure TPA with synergy index of up to 2.7 and increase in K_{ads} to 0.07 mM^{-1}. High mass productivity was evident by a specific degradation rate of 2.236 $mmol.g^{-1}.h^{-1}$ for WT8 at 1.0 mM of dye, proving the exceptional effectiveness on these hybrids in treating dense industrial pollution load.

References

[1] Choi JH. Redox Properties of Heteropolyacid Catalysts Probed by Electrochemical Analysis, UV-visible Spectroscopy and Scanning Tunneling Microscopy, PhD Thesis, Seoul National Universiy 2015.

[2] Misono M. Catalysis of Heteropoly Compounds (Polyoxometalates). Studies in Surface Science and Catalysis 2013:97-155.

[3] Cui L, Zhang S, Zhao Y, Ge X, Yang L, Li K, Feng L, Li R, Chen J. Tunable multi-electron redox polyoxometalates for decoupled water splitting driven by sunlight. Nature Communications 2025;16(1):3674.

[4] Qiu X, Wang R. Polyoxometalate-Based Photocatalytic New Materials for the Treatment of Water Pollutants: Mechanism, Advances, and Challenges. Catalysts 2025;15(7):613.

[5] Li N, Wang X, Jin Z, Liu H, Liu Y, Zhang L, Jin X, Zhang J, Fei P. Three Isostructural Keggin-Type Polyoxometalate Hybrids for Effective Dye Degradation. Applied Organometallic Chemistry 2025;39(12):e70442.

[6] Man C, Xu C, Wang J, Li X, Li T, Ma Y, Zhang S, Qiao Y, Wu Q. Mechanistic study on the photocatalytic degradation of rhodamine B via Mn–Schiff-base-modified Keggin-type polyoxometalate composite materials. RSC Advances 2025;15(16):12364-12371.

[7] Zheng S, Zhang J, Li X, Fang W, Yang G. Cubic Polyoxometalate−Organic Molecular Cage. Journal of the American Chemical Society 2010;132(43):15102-15103.

[8] Macht J, Janik M, Neurock M, Iglesia E. Mechanistic Consequences of Composition in Acid Catalysis by Polyoxometalate Keggin Clusters. Journal of the American Chemical Society 2008;130(31):10369-10379.

[9] Misra A, Kozma K, Streb C, Nyman M. Beyond Charge Balance: Counter-Cations in Polyoxometalate Chemistry. Angewandte Chemie International Edition 2019;59(2):596-612.

[10] Shah S, Bibi S, Ali K, Bibi I, Zafar O, Begum S. Mechanochemical synthesis of ionic solids based on phosphotungstic acid and triethylamine for photocatalytic dye degradation. Physica Scripta 2023;98(11):115010.

[11] Dias J, Osegovic J, Drago R. The Solid Acidity of 12-Tungstophosphoric Acid. Journal of Catalysis 1999;183(1):83-90.

[12] Martinelli A, Otero-Mato J, Garaga M, Elamin K, Rahman S, Zwanziger J, Werner-Zwanziger U, Varela L. A New Solid-State Proton Conductor: The Salt Hydrate Based on Imidazolium and 12-Tungstophosphate. Journal of the American Chemical Society 2021;143(34):13895-13907.

[13] Li R, Wang Y, Zeng F, Si C, Zhang D, Xu W, Shi J. Advances in Polyoxometalates as Electron Mediators for Photocatalytic Dye Degradation. International Journal of Molecular Sciences 2023;24(20):15244.

[14] Turchi C. Photocatalytic degradation of organic water contaminants: Mechanisms involving hydroxyl radical attack. Journal of Catalysis 1990;122(1):178-192.

[15] Mills A, O'Rourke C, Moore K. Powder semiconductor photocatalysis in aqueous solution: An overview of kinetics-based reaction mechanisms. Journal of Photochemistry and Photobiology A: Chemistry 2015;310:66-105.

[16] Entezami N, Farhadian M, Nazar A. Synergistic effects of electric current and GAs/Bi_2O_3/ZIF-67 photocatalysis on graphite in a planar microreactor applied for tetracycline degradation and kinetic pathway analysis. Scientific Reports 2025;15(1):27644.

[17] Kampouri S, Nguyen T, Spodaryk M, Palgrave R, Züttel A, Smit B, Stylianou K. Dual-Functional Photocatalysis: Concurrent Photocatalytic Hydrogen Generation and Dye Degradation Using MIL-125-NH2 under Visible Light Irradiation (Adv. Funct. Mater. 52/2018). Advanced Functional Materials 2018;28(52):1806368.

[18] Ren Y, Wang M, Chen X, Yue B, He H. Heterogeneous Catalysis of Polyoxometalate Based Organic–Inorganic Hybrids. Materials 2015;8(4):1545-1567.

[19] Kondratenko Y, Nikonorova A, Zolotarev A, Ugolkov V, Kochina T. Tris(hydroxymethyl)methyl ammonium salts of biologically active carboxylic acids. Synthesis, properties and crystal structure. Journal of Molecular Structure 2020;1207:127813.

[20] Hidalgo G, Devillers M, Gaigneaux E. Hybrid Materials Based on Keggin Phosphotungstate and Bipyridine with Valuable Hydrophobic and Redox Properties. Inorganic Chemistry 2022;61(32):12494-12507.

[21] Heacock R, Marion L. The infrared spectra of secondary amines and their salts. Canadian Journal of Chemistry 1956;34(12):1782-1795.

[22] Alharthi A. Efficient Catalytic Performance of Calcined Tungstophosphoric Acid for the Claisen-Schmidt Condensation under Solvent-Free Reaction. Asian Journal of Chemistry 2019;31(11):2579-2584.

[23] Stoyanov E, Reed C. IR Spectrum of the H5O2+ Cation in the Context of Proton Disolvates L−H+−L. The Journal of Physical Chemistry A 2006;110(48):12992-13002.

[24] Bera M, Antonio M. Aggregation of Heteropolyanions Implicates the Presence of Zundel Ions Near Air-Water Interfaces. ChemistrySelect 2016;1(10):2107-2112.

[25] Edwards J, Thiel C, Benac B, Knifton J. Solid-state NMR and FT-IR investigation of 12-tungstophosphoric acid on TiO2. Catalysis Letters 1998;51(1-2):77-83.

[26] Kammert J, Brezicki G, Miyake N, Stavitski E, Davis R. Reduction of Propanoic Acid over Pd-Promoted Supported WOx Catalysts. ChemCatChem 2019;12(1):314-325.

[27] Iftikhar T, Rosnes M. Covalent organic-inorganic polyoxometalate hybrids in catalysis. Frontiers in Chemistry 2024;12:1447623.

[28] Samruddhi M, Bhatkar A, Prabu M, Mekala S, Gogoi P, Mohapatra G, Thirumalaiswamy R. Selective O-alkylation of Phenol Using Dimethyl Ether. Reactions 2022;3(4):602-614.

[29] Chen L, Bai B. Facile Preparation of Phosphotungstic Acid-Impregnated Yeast Hybrid Microspheres and Their Photocatalytic Performance for Decolorization of Azo Dye. International Journal of Photoenergy 2013;2013:1-9.

[30] Liu Q, Wang X. Polyoxometalate Clusters: Sub-nanometer Building Blocks for Construction of Advanced Materials. Matter 2020;2(4):816-841.

[31] Aguilera Palacios E, Palermo V, Sathicq A, Pizzio L, Romanelli G. A New Series of Tungstophosphoric Acid-Polymeric Matrix Catalysts: Application in the Green Synthesis of 2-Benzazepines and Analogous Rings. Catalysts 2022;12(10):1155.

[32] Li P, Liu Z, Tu S, Jiang W, Yang J. Ammonium phosphotungstate nanoparticle/ultrathin g-C3N4 composite photocatalysts with Z-scheme heterojunctions: preparation and application to organic contaminant degradation. Materials Research Express 2023;10(6):065501.

[33] Chernyak A, Chub A, Sanginov E, Barzilovich P. An NMR study of nanostructured ammonium 12-phosphotungstate. Russian Chemical Bulletin 2013;62(8):1798-1802.

[34] Lee G, Lee C, Kim H, Jeon Y, Shul Y, Park J. Bifunctional 1,2,4-Triazole/12-Tungstophosphoric Acid Composite Nanoparticles for Biodiesel Production. Nanomaterials 2022;12(22):4022.

[35] Patyk-Kaźmierczak E, Izquierdo-Ruiz F, Lobato A, Kaźmierczak M, Moszczyńska I, Olejniczak A, Recio J. The curious case of proton migration under pressure in the malonic acid and 4,4′-bipyridine cocrystal. IUCrJ 2024;11(2):168-181.

[36] Expósito-Gálvez J, Vattier F, Pedrosa J, Carrillo-Carrión C, Oskam G. Tuning the Photoelectrochemical Properties of Ti/W-Modified PCN-222 Using Charge–Selective Interfaces. ACS Applied Materials & Interfaces 2026;18(6):9877-9891.

[37] Mustapha S, Ndamitso M, Abdulkareem A, Tijani J, Shuaib D, Mohammed A, Sumaila A. Comparative study of crystallite size using Williamson-Hall and Debye-Scherrer plots for ZnO nanoparticles. Advances in Natural Sciences: Nanoscience and Nanotechnology 2019;10(4):045013.

[38] Choubisa B, Dholakiya B, Patel M. Synthesis and Characterization of Polylactic Acid (PLA) by Using SSA, CSA and TPA Type Solid Acid Catalyst System in Polycondensation Method. Journal of Macromolecular Science, Part A 2013;50(8):828-835.

[39] Ilhan S, Kalpakli A, Kahruman C, Yusufoglu I. The investigation of thermal decomposition mechanism of ammonium phosphotungstate hydrate in inert gas atmosphere. Thermochimica Acta 2012;546:1-7.

[40] Marosi L, Escalona Platero E, Cifre J, Otero Areán C. Thermal dehydration of H3 + xPVxM12 − xO40·yH2O Keggin type heteropolyacids; formation, thermal stability and structure of the anhydrous acids H3PM12O40, of the corresponding anhydrides PM12O38.5 and of a novel trihydrate H3PW12O40·3H2O. Journal of Materials Chemistry 2000;10(8):1949-1955.

[41] da Silva M, Rodrigues A, Lopes N. Keggin Heteropolyacid Salt Catalysts in Oxidation Reactions: A Review. Inorganics 2023;11(4):162.

[42] Gildo P, Dugos N, Roces S, Wan M. Optimized Ultrasound-Assisted Oxidative Desulfurization Process of Simulated Fuels over Activated Carbon-Supported Phosphotungstic Acid. MATEC Web of Conferences 2018;156:03045.

[43] Lan J, Wang Y, Huang B, Xiao Z, Wu P. Application of polyoxometalates in photocatalytic degradation of organic pollutants. Nanoscale Advances 2021;3(16):4646-4658.

[44] Liu C, Zheng T, Liu S, Zhang H. Photodegradation of malachite green dye catalyzed by Keggin-type polyoxometalates under visible-light irradiation: Transition metal substituted effects. Journal of Molecular Structure 2016;1110:44-52.